Materials Characterization 99 (2015) 118–127

Contents lists available at ScienceDirect

Materials Characterization

journal homepage: www.elsevier.com/locate/matchar

Investigation of deformation micro-mechanisms in nickel consolidated from a bimodal powder by spark plasma sintering

D. Tingaud [a], P. Jenei [b], A. Krawczynska [c], F. Mompiou [c], J. Gubicza [b], G. Dirras [a,*]

[a] Université Paris 13, Sorbonne Paris Cité, LSPM, CNRS, 99 Avenue J.B. Clément, 93430 Villetaneuse, France
[b] Department of Materials Physics, Eötvös Loránd University Budapest, P.O.B. 32, H-1518, Hungary
[c] Université de Toulouse and CEMES, CNRS, 29 rue Jeanne Marvig, 31055 Toulouse, France

ARTICLE INFO

Article history:
Received 7 October 2014
Received in revised form 8 November 2014
Accepted 11 November 2014
Available online 20 November 2014

Keywords:
Nickel
Spark plasma sintering
Bimodal structure
Dislocation
In-situ TEM

ABSTRACT

Bulk polycrystalline nickel compact was processed by spark plasma sintering from heterogeneous powder consisting of a mixture of nanometer and micrometer sized particles. The consolidated samples inherited the bimodal structure of the starting powder and was composed of ~55 vol.% coarse-grained (with the grain size larger than 1 μm) and ~45 vol.% ultrafine-grained (with an average grain size of ~550 nm) components. The deformation mechanisms were established by EBSD, X-ray line profile analysis and in-situ TEM observations. In the ultrafine-grained volume, the deformation occurred mainly through the activation of dislocation sources emitting full or partial dislocation either from grain interior or grain boundaries. Besides dislocation activity, rolling and sliding of nanograins were also observed during deformation by in-situ transmission electron microscopy, which have a considerable contribution to the observed high strain rate sensitivity of the bimodal microstructure. The cracks formed during deformation easily propagated in the nanograin regions due to the weaker particle bonding caused by the relatively high fraction of native oxide layer on the surface of the initial nanoparticles.

1. Introduction

Microstructures with enhanced mechanical properties are generally obtained by means of grain size reduction, development of multi-modal grain size distribution, and tailoring grain boundary (GB) structure. Indeed, it is well known that nanocrystalline (NC) and ultrafine-grained (UFG) materials have superior mechanical strengths compared to their conventional coarse-grained (CG) counterparts [1–4]. Among the several ways of processing of bulk materials with NC or UFG microstructure, the compaction of powders [1–5] has a fundamental place due to its versatility in tailoring in-demand composite-like microstructures. This type of process enables to obtain centimeter-scale and fully dense materials with different grain sizes spanning the nanometer (30–100 nm) range to the UFG (100–1000 nm) regime and above [3,4].

Recently, much attention has been paid to the novel spark plasma sintering (SPS) consolidation technique [6,7]. The most important advantages of the SPS processing route compared to conventional consolidation methods are the much shorter duration and the lower temperature of processing, which limit grain-growth during consolidation [8].

NC materials have so far demonstrated enhanced mechanical characteristics, such as high strength and fracture stress. Nevertheless, other key properties such as ductility, which is very important in forming processes, still needs to be improved. In that context, different strategies have been proposed to offset the low tensile ductility accompanying the high flow stress of NC and UFG materials [9,10]. For instance, it has been demonstrated that controlled volume fraction of twins in Cu induces both high strength and considerable tensile ductility, the latter being due to the strain rate sensitivity improvement by the presence of coherent twin boundaries (TBs) [11–14]. Another strategy for the improvement of ductility of NC and UFG materials is the incorporation of coarse grains in a fine-grained matrix [9,15–17]. In this case, the improvement of ductility can be attributed to the larger dislocation activity (mobility and storage) in coarse grains, thereby enhancing the strain hardening capability of materials [18]. The bimodal grain-structure can be achieved by heterogeneous grain-growth in severely deformed materials [19–21] or via abnormal grain-growth caused by microstructure heterogeneities such as inhomogeneous solute distribution and/or residual porosity [22]. Although in some cases the magnitude of the improvement of ductility does not meet the high expectations raised [23], the processing of bimodal microstructures is still often suggested in order to improve the mechanical response of metallic materials [9,18,24,25]. Our previous studies have demonstrated the successful processing of bimodal microstructures in Ni by SPS [17] and studied their mechanical performance under impact loading [25]. However, the deformation mechanisms in the CG and UFG volumes during quasistatic deformation have not been identified yet.

In the present work we investigate the room temperature (RT) quasistatic plastic behavior of an SPS-processed polycrystalline Ni

* Corresponding author.
E-mail address: dirras@univ-paris13.fr (G. Dirras).

http://dx.doi.org/10.1016/j.matchar.2014.11.025
1044-5803/

with bimodal grain-structure at different strain rates. The underlying deformation mechanisms are revealed by post-mortem EBSD and X-ray diffraction (XRD) experiments, as well as by in-situ TEM investigations. The results may yield a better understanding of the contributions of the different components in a heterogeneous grain structure to the mechanical performance.

2. Materials and procedures

2.1. SPS processing

Bulk Ni samples were consolidated by SPS. The starting high purity (>99.8 wt.%) Ni powder was fabricated by electro-explosion of wire (Argonide Corporation, Stanford, USA) [26]. The sintering of the powder during SPS is assisted by the simultaneous application of direct current pulses of very high intensity (several thousands of amperes) and a uniaxial pressure exerted on the encapsulating system [27]. In the present case, the Ni powder was sintered by the SPS apparatus (model 515S-SYNTEX) located at the regional SPS platform facility hosted by ICMPE (Thiais, France). More details have been given elsewhere [28]. For the present study, SPS processing was carried out at a temperature of 600 °C for 15 min. The dwell pressure during sintering was set as 100 MPa. The relative density of the bulk sample was evaluated by the method based on the Archimedes principle and yielded a value of about 98%.

2.2. Mechanical properties

Following sintering, the macroscopic mechanical behavior was studied by means of uniaxial compression at room temperature and two different strain rates of $2 \times 10^{-4}\,s^{-1}$ and $2 \times 10^{-2}\,s^{-1}$ in order to investigate the effect of strain rate on deformation behavior. For compression tests, prismatic samples (3 mm × 3 mm × 5 mm) were mechanically cut from the compacted material and tested using an Instron universal machine (model 1195) with a 10 kN maximum capacity load cell. The strain was computed from the crosshead displacement corrected for the stiffness of the machine.

2.3. Microstructure study of the as-consolidated specimen and post-mortem analyses of the deformed sample

The microstructure of the as-consolidated and the subsequently deformed Ni samples was studied by X-ray line profile analysis. The X-ray line profiles were measured by a high-resolution rotating anode diffractometer (type: RA-MultiMax9, manufacturer: Rigaku) using $CuK\alpha_1$ ($\lambda = 0.15406$ nm) radiation. Two-dimensional imaging plates detected the Debye–Scherrer diffraction rings. The line profiles were determined as the intensity distribution perpendicular to the rings obtained by integrating the two dimensional intensity distribution along the rings. The line profiles were evaluated by the extended Convolutional Multiple Whole Profile (eCMWP) fitting procedure [29,30]. In this method, the diffraction pattern is fitted by the sum of a background spline and the convolution of the instrumental pattern and the theoretical line profiles related to the crystallite size, dislocations and twin faults. The details of the eCMWP fitting procedure can be found in Refs. [29,30]. Because of the ultrafine-grained microstructure of the studied samples, the physical broadening of the profiles was much higher than the instrumental broadening. Therefore, instrumental correction was not applied in the evaluation. The eCMWP method gives the area-weighted mean crystallite size ($\langle x \rangle_{area}$), the dislocation density (ρ) and the twin boundary probability (β) with good statistics, where the twin boundary probability is defined as the fraction of twin boundaries among the {111} lattice planes. The area-weighted mean crystallite size was calculated from the median (m) and the lognormal variance (σ^2) of the assumed lognormal crystallite size distribution as: $\langle x \rangle_{area} = m \cdot \exp(2.5\sigma^2)$. Additionally, a parameter denoted by q describing the edge/screw character of dislocations is also obtained from the eCMWP fitting.

EBSD investigations were carried out using a Zeiss Supra 40VP FEG scanning electron microscope (SEM). Depending on the size of the observed entities, the areas of scanned regions during EBSD experiments were adequately adapted using a step size between neighboring measurement positions from 50 to 250 nm. The average grain size, the fractions of low angle grain boundaries (LAGBs), high angle grain boundaries (HAGBs) and special Σ3 boundaries were extracted from the EBSD scans using OIM software version 5 from TexSem Laboratories (TSL).

2.4. In-situ transmission electron microscopy experiments

In-situ TEM was used to investigate the deformation mechanisms within the UFG component of the microstructure during tension. Specimens were prepared from the bulk material, first by cutting 3 mm × 1 mm × 0.5 mm rectangles that were eventually mechanically ground. The rectangles were then either thinned till perforation by electropolishing or by a combination of ion milling using Precision Ion Polishing System (PIPS™, Gatan, Inc., Model 691) and a "flash polishing" using an A2 electropolishing solution from Struers at a voltage of 7 V for 5 s at RT [31]. The latter sample preparation route was applied in order to remove the damaged surface layer caused by ion milling as a consequence of the faster etching rate of the UFG volumes compared to the CG ones during electropolishing. The samples were subsequently glued to a copper grid and placed into a Gatan straining holder. The in-situ TEM experiments were carried out in a JEOL 2010HC microscope operated at 200 kV. A MEGAVIEW III camera operating at a rate of 25 fps recorded the TEM images during deformation. The investigated areas were located on two sides of the hole in the perforated sample where the local stress is maximal [32].

To complement in-situ TEM observation, Automated Crystallographic Orientation Mapping (ACOM) in TEM was performed using the ASTAR technique [33]. The orientation maps were produced by a CM20FEG microscope operated at 200 kV.

3. Results and discussion

3.1. Microstructure of the starting powder and the sintered material

Fig. 1 shows a SEM micrograph of the initial Ni powder. The powder comprises spherical nanoparticles with the diameter between 50 and 100 nm in addition to ultrafine-grained and micrometer-sized particles (up to the size of 5 μm). Therefore, the initial powder has a bimodal particle structure.

After sintering, the microstructure of the as-consolidated sample was described as an ensemble of CG (the grain size is larger than 1 μm) and UFG (the grain size is smaller than 1 μm) volumes, i.e. as a bimodal microstructure. The as-processed bimodal-like microstructure is illustrated in Fig. 2, showing a map in which the various colors indicate the grains classified into different size ranges. The fractions of CG and UFG volumes computed from several EBSD images (Fig. 2 is only one of them) were found to be ~55 and ~45 vol.%, respectively. The average grain size in the UFG component of the microstructure was ~550 nm. In addition to quasi-random crystallographic texture (not shown), EBSD investigations showed that the CG entities can be subdivided into isolated micrometer-sized grains with an average grain size of ~2 μm and larger spherical multi-crystalline aggregates consisting of more than one coarse grain (see Figs. 2 and 3a). Actually, the isolated grains with an average grain size of ~2 μm and the spherical multi-crystalline clusters with the size up to ~30 μm occupy 51 and 4 vol.% of the whole microstructure, respectively. The average grain size within the multi-crystalline clusters is ~10 μm. Another characteristic feature of the microstructure is the high fraction of Σ3 CSL-type boundaries, appearing as red lines in both CG and UFG components in Fig. 3a. Such an

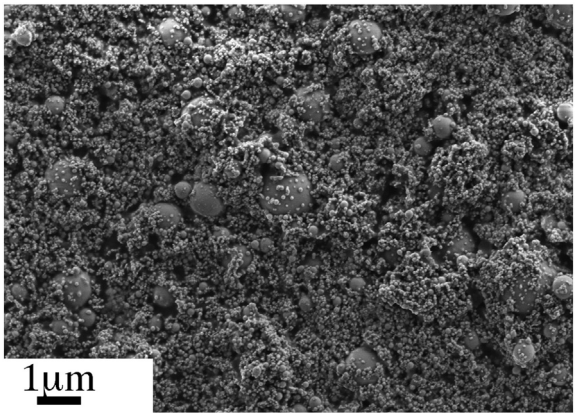

Fig. 1. The bimodal-like structure of the initial powder observed by SEM.

observation has also been reported in a previous work [28]. The misorientation angle distributions in the UFG and CG fractions are similar, as shown in Fig. 3b. The peak appearing at the angle of about 60° indicates the high fraction of Σ3 boundaries in both regions. The Σ3 boundaries include coherent twin boundaries as it can be seen within the UFG component or the large multi-crystalline cluster shown in Fig. 3a.

The UFG component comprises nanograins (NGs) with the size between 50 and 100 nm and larger grains with the size between 100 nm and 1 µm, as illustrated in Fig. 4. It should be noticed that residual porosity is mostly found in the UFG volumes, probably due to the incomplete bonding between the initial nanoparticles. Indeed, Scanning Transmission Electron Microscopy–Energy Dispersive Spectroscopy (STEM–EDS) measurements (see Fig. A of Supplementary figure) revealed an increase of the oxygen content (locally up to 10%) in the area containing very small grains (~10–20 nm) close to the crack compared to the area containing larger grains (CG or UFG), which is most probably related to

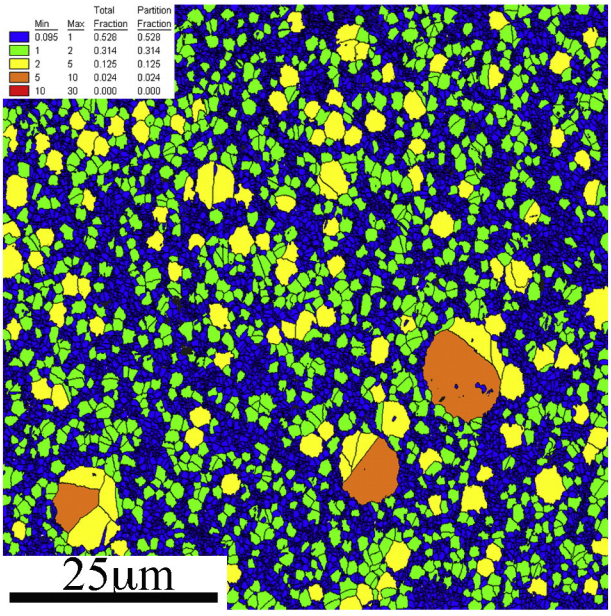

Fig. 2. EBSD (superimposed IPF and boundary maps) image of the SPS processed sample. The grain size distribution is shown by the inset. The blue color represents the UFG component of the microstructure. (For interpretation of the references to color in this figure legend, the reader is referred to the web version of this article.)

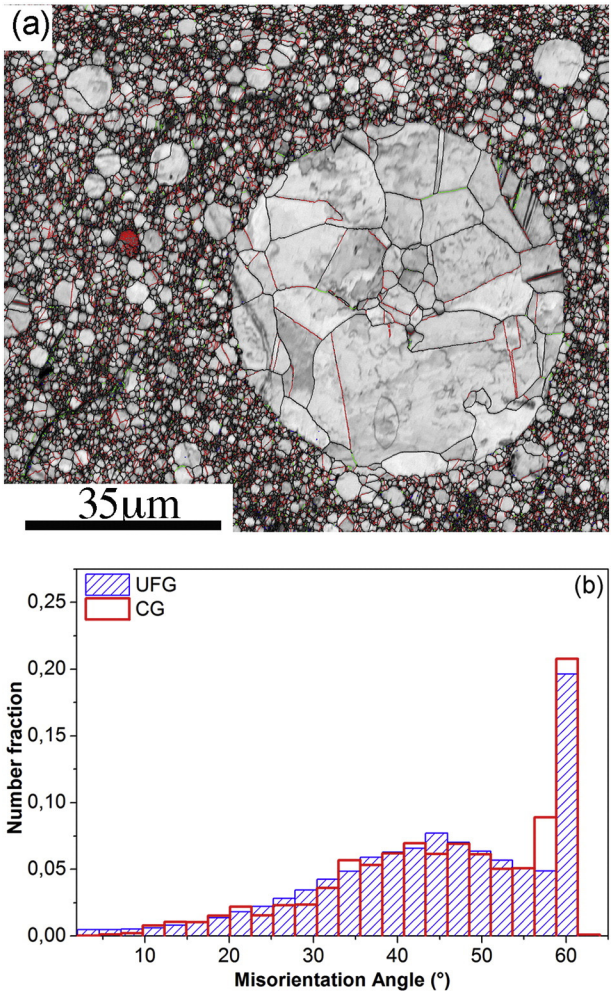

Fig. 3. Superimposed boundary map/IQ images showing a large multi-crystalline cluster of about 50 µm in diameter (a); distribution of misorientation across boundaries in UFG and CG components of the microstructure (b). Red lines in (b) correspond to Σ3 CSL-type boundaries. (For interpretation of the references to color in this figure legend, the reader is referred to the web version of this article.)

the higher amount of NiO phase, originated from the native NiO layer on the surface of the nanoparticles. This oxide phase hinders consolidation of nanoparticles, leading to a large local porosity. Actually, the phase composition in the as-consolidated sample was studied by XRD using the same device as for XLPA. As illustrated in Fig. 5, a small amount of NiO phase (PDF: 44-1159) was identified in addition to the main phase of fcc Ni. The ratio of the summed integrated intensities for NiO and Ni peaks was 3.0 ± 0.5%. The presence of incomplete sintering between NGs has a strong impact on the mechanical properties as observed and discussed below.

3.2. The mechanical behavior during compression

Fig. 6 shows the engineering stress–strain curves obtained during uniaxial compression of the consolidated sample at room temperature. The curves labeled as (C1) and (C2) correspond to the strain rates of $2 \times 10^{-4}\ s^{-1}$ and $2 \times 10^{-2}\ s^{-1}$, respectively. The higher strain rate resulted in a significant hardening, while at the lower strain rate the sample softened just after the strain of ~10%. The maximum value of the stress (i.e. the compressive strength) increased from about 600 MPa to 930 MPa when the strain rate was raised from $2 \times 10^{-4}\ s^{-1}$ to $2 \times 10^{-2}\ s^{-1}$. In addition, due to the higher work hardening the strain

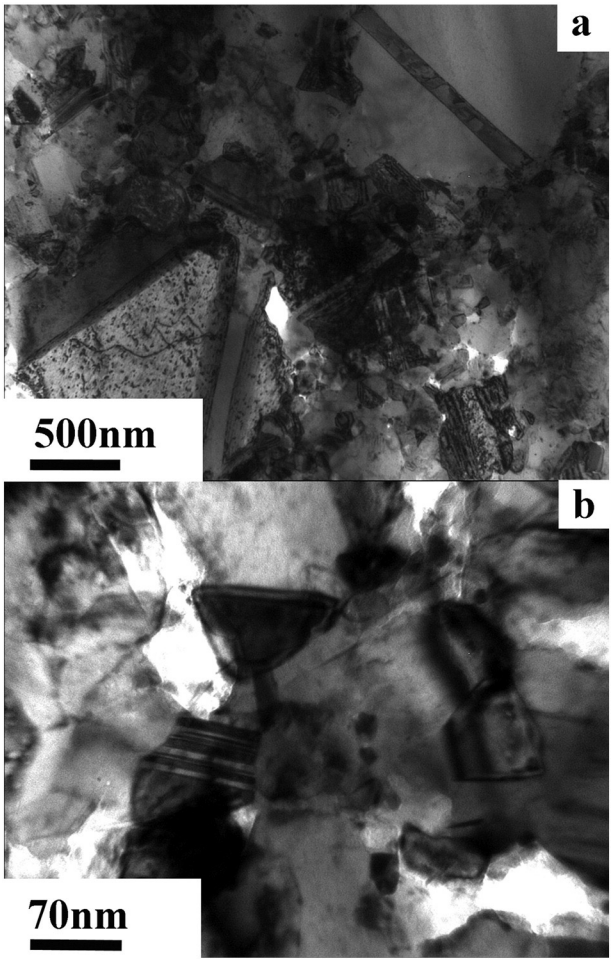

Fig. 4. TEM bright field micrographs of the initial bulk sample showing the typical features of the UFG component (a, b). b shows the presence of nanograins (grain size < 100 nm) and the associated porosity due to incomplete particle bonding.

corresponding to the compressive strength is larger (~70%) at the higher strain rate than the value (~10%) characteristic for the lower rate. These observations are in good agreement with previous works [9,24]. In particular, the increase of strain rate and the processing of a bimodal microstructure have been suggested as two possible strategies to

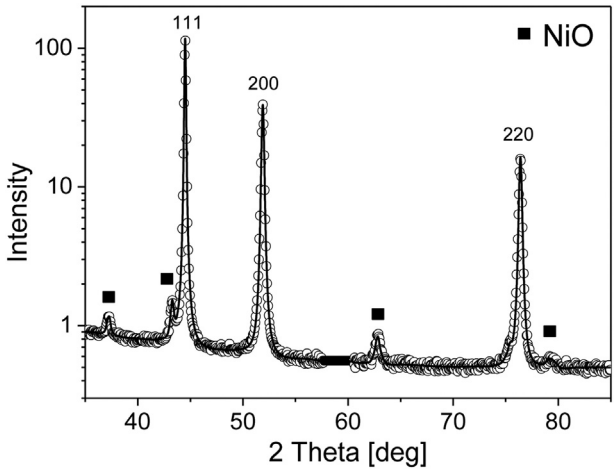

Fig. 5. eCMWP fitting for sample A (after compression up to the strain of 32%). The open circles and the solid line represent the measured data and the fitted curves, respectively. The patterns are in logarithmic intensity scales in order to clearly show the weak peaks of NiO.

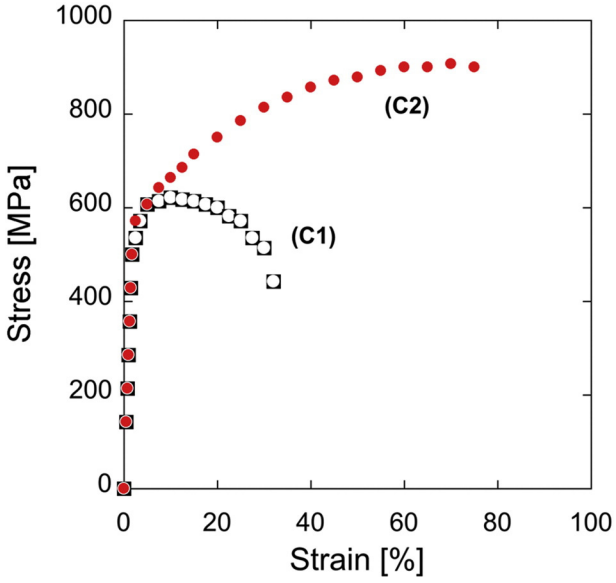

Fig. 6. Stress–strain curves after compression tests conducted at RT. (C1): the strain rate is $2 \times 10^{-4}\ s^{-1}$; (C2): the strain rate is $2 \times 10^{-2}\ s^{-1}$. See text for more details.

postpone the onset of deformation instability, thus improving the ductility of UFG materials [9].

Fig. 7a–d shows EBSD investigations illustrating the deformation characteristics of the samples deformed at the two strain rates of $2 \times 10^{-4}\ s^{-1}$ (Fig. 7a–b) and $2 \times 10^{-2}\ s^{-1}$ (Fig. 7c–d) up to the failure point, corresponding to 32 and 65%, respectively. For both strain rates, the microstructure characteristics are similar when viewed from the normal face (perpendicular to the compression direction) as shown in Fig. 7a–c: the morphology of the grains is the same and the CG entities are free from any kind of deformation patterning (in the present conditions of EBSD analysis). LAGBs with misorientation in the range of 2–5° (blue color in the EBSD map) and 5–15° (green color in the EBSD map) appear mostly in the vicinity of grain interfaces, due to localized deformation at these regions. The fraction of LAGBs is only slightly larger for the higher strain rate at the failure than for the lower strain rate as it can be seen in Fig. B of Supplementary figure. Therefore, it can be concluded from the EBSD investigations that despite the difference in strain rate and strain to failure, the microstructure in the two samples is quasi-similar when it is investigated on the normal faces. This is in line with XRD analysis presented in Section 3.3. However, EBSD investigations carried out on the transverse face (parallel to the compression direction) reveal differences between the microstructures compressed at two different strain rates (and strains), as shown in Fig. 7b–d. For the lower strain rate the grains are only slightly elongated while for the higher strain rate heavily flattened grains with high aspect ratio are observed. This difference can be explained by the larger strain to failure for the case of higher strain rate. The EBSD data also show dislocation patterning within CGs and reveal the presence of LAGBs with misorientation lower than 2° in the flattened grains (gray contrast in CGs). In addition, the fraction of LAGBs with misorientation between 5 and 15° also increased due to compression, particularly in the sample deformed at $2 \times 10^{-2}\ s^{-1}$ (Fig. 7d). These changes of the grain misorientation distribution during deformation suggest dislocation activity, especially in CGs of the consolidated microstructure.

To complement these observations, crystal orientation maps using the ASTAR technique were acquired. Fig. 8a–c shows bright field TEM micrographs and the corresponding inverse pole figure (IPF) + index quality (IQ) maps for the sample deformed at $2 \times 10^{-2}\ s^{-1}$ up to failure (65%). These images were obtained on the normal face. This very local view, contrary to the EBSD map taken on the same face (see Fig. 7c), suggests that the microstructure consists of elongated grains. In

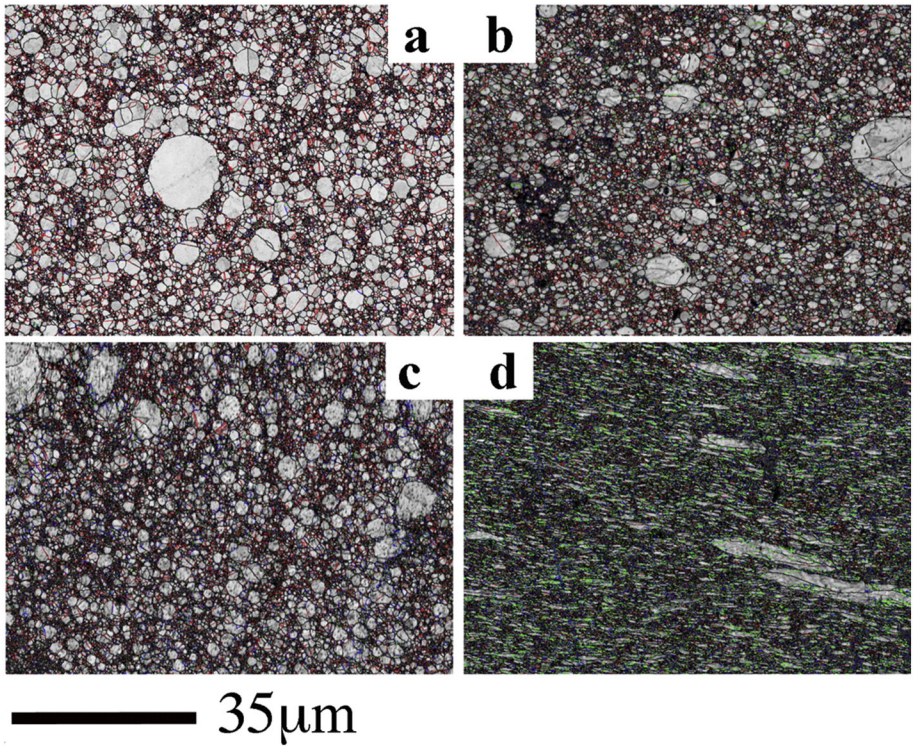

Fig. 7. EBSD images showing the microstructures after deformation to failure at two different strain rates. a and b were obtained at the strain of 32% and the strain rate of $2 \times 10^{-4}\ s^{-1}$ on the planes perpendicular and parallel to the compression direction, respectively. c and d were taken at the strain of 65% and the strain rate of $2 \times 10^{-2}\ s^{-1}$ on the planes perpendicular and parallel to the compression direction, respectively.

addition, spherical NGs are clearly visible between UFG grains, similar to the as-consolidated state (see the TEM images in Fig. 4). In many areas, NGs form thin layers following the contours of the UFG grains. It is interesting to note that the orientation inside the UFG grains (see for instance grain A in Fig. 8b) is not always uniform, suggesting high density of dislocations presumably arranged into LAGBs as discussed above, in agreement with XRD investigations presented in the next section. The spherical shape of a large number of NGs between elongated grains in the deformed material suggests that their interiors did not deform plastically but rather the grains rolled, rotated and/or glided collectively along their boundaries in order to accommodate plastic strain. Most probably, in this process the pores between NGs act as "free volumes", thereby facilitating the deformation. The rheological behavior of the NG component is then thought to have a significant impact on the mechanical response, especially on the hardening/softening behavior.

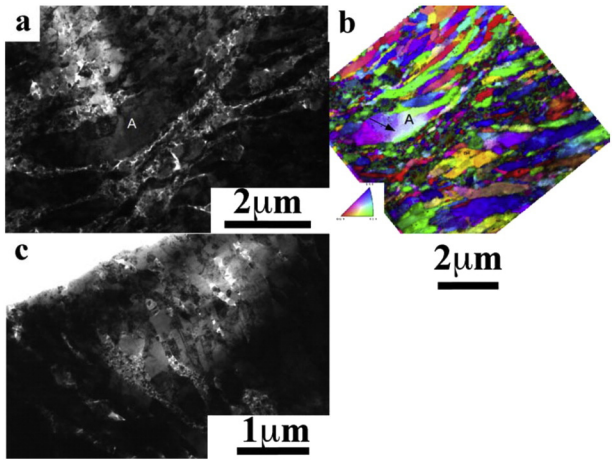

Fig. 8. TEM bright field images of the microstructure in the plane perpendicular to the loading axis deformed at $2 \times 10^{-2}\ s^{-1}$ (a, b) and $2 \times 10^{-4}\ s^{-1}$ (c). Note the presence of elongated grains surrounded by NGs in both cases. The IPF map (a) highlights the presence of local misorientation in the elongated grains (indicated by an arrow in grain A) due to subgrain boundaries and/or high dislocation density.

3.3. XRD study of the change in lattice defect structure during deformation

The study of the change in the type and densities of lattice defects (dislocations, twin boundaries, etc.) during deformation may indicate the main deformation mechanisms that occurred during plastic straining. Therefore, the parameters of the microstructure were determined before and after compression at both strain rates.

The median and the lognormal variance of the crystallite size distribution, the area-weighted mean crystallite size, the dislocation density and the twin boundary probability determined by X-ray line profile experiments are listed in Table 1. For the initial state, as shown in Fig. 9, the Debye–Scherrer rings exhibited inhomogeneous intensity distribution. The sharp intensity spots in the Debye–Scherrer rings are related to reflecting grains in the CG fraction. The diffraction peaks of these large grains were as narrow as the instrumental profiles ($\Delta(2\Theta) = 0.02°$), therefore these lines were not evaluated for the microstructure. However, it can be established that the dislocation density and the crystallite size are smaller and larger, respectively, in the CG volumes than the detection limits for the present experimental setup of X-ray line profile analysis ($10^{13}\ m^{-2}$ and 800 nm, respectively). For the determination of the microstructural parameters in the UFG volume, parts of the Debye–Scherrer rings free from sharp spots were cut and evaluated. Therefore, for the initial sample the parameters of the microstructure presented in Table 1 characterize only the UFG fractions. In the whole volume of the initial sample, the dislocation density and the crystallite size were lower and larger, respectively, than the values given in Table 1. At the same time, for the deformed samples high intensity spots were not visible as the large density of dislocations formed during compression and the grain fragmentation considerably increased the peak profile breadths of coarse grains. As a consequence, in the case of

Table 1
The parameters of the microstructure obtained by X-ray line profile analysis. m and σ^2 are the median and the lognormal variance of the log-normal crystallite size distribution, $\langle x \rangle_{area}$ is the area-weighted mean crystallite size, ρ is the dislocation density and β is the twin boundary probability.

Sample	m [nm]	σ^2	$\langle x \rangle_{area}$ [nm]	ρ [10^{14} m^{-2}]	β [%]
Initial sample (UFG regime only)	175 ± 15	0.023 ± 0.005	185 ± 20	1.2 ± 0.2	0.5 ± 0.1
After compression up to the strain of 32% at the strain rate of 10^{-4} s^{-1} (whole sample)	34 ± 4	0.16 ± 0.03	51 ± 6	22 ± 2	0.1 ± 0.1
After compression up to the strain of 65% at the strain rate of 10^{-2} s^{-1} (whole sample)	37 ± 4	0.12 ± 0.03	50 ± 6	25 ± 3	0.2 ± 0.1

the deformed samples the parameters of the microstructure listed in Table 1 describe the whole material.

The dislocation density increased by about one order of magnitude while the twin boundary probability decreased during compression, which indicates that the deformation in the consolidated samples occurred mainly by the motion and multiplication of dislocations. The experimental value of parameter q was 1.9 for both strain rates. This quantity reflects the edge/screw character of dislocations. The theoretically calculated values of q for pure edge and screw dislocations in Ni are 1.4 and 2.2, respectively [34], therefore the measured q suggests a mixed (half edge–half screw) character of dislocations. The decrease of the twin boundary probability can be attributed to the interaction between gliding dislocations and twin boundaries, which resulted in an un-twinning process as described in a previous report [35]. The crystallite size distributions for the initial sample and its deformed counterparts are plotted in Fig. 10. Significant reduction in the mean crystallite size by a factor of about four occurred during compression at both strain rates.

The values of the crystallite size, the dislocation density and the twin boundary probability agree within the experimental error for the two strain rates. At the same time, the flow stress values are very different: about 500 and 900 MPa for the strain of 32% at the strain rate of 2×10^{-4} s^{-1} and for the strain of 65% at the strain rate of 2×10^{-2} s^{-1}, respectively (see Fig. 6). As these strain rates are too low for the occurrence of dislocation drag effects, the large increment in the flow stress at higher strain rate can be, at least partly, explained by the operation of deformation processes with large strain rate sensitivity. Dislocation nucleation at grain boundaries and grain-boundary sliding [36,37] are two possible mechanisms which may result in the increase in strain rate sensitivity. More generally, the interaction between dislocations and twin/grain boundaries, including dislocation absorption, decomposition and motion, can be invoked as potential mechanisms yielding high strain rate sensitivity. These mechanisms are in line with in-situ TEM investigations (see the next section). Nevertheless, it should also be emphasized that besides these mechanisms, intragranular dislocation mechanisms also operate as indicated by the strong increase of the dislocation density during compression.

3.4. In-situ TEM investigations

In order to get a precise identification of the operating deformation mechanisms in the present bimodal microstructure, in-situ TEM experiments have been carried out. Indeed, in-situ TEM study of the microstructure during tensile test shows that various mechanisms can be distinguished in the UFG component of the consolidated material. These mechanisms are the followings: crack nucleation and propagation, grain sliding/rolling, lattice dislocation activity, mechanical twinning and enhanced partial dislocation activity.

3.4.1. Crack development, growth and propagation

The development of a crack can be seen in the TEM image of Fig. 11, which was taken during an in-situ TEM experiment. Fig. 11a and b shows that the crack propagates in the volumes where the porosity is large, and opens the existing porosities in front of its tip. Fig. 11c shows the orientation map superimposed on the IQ map before crack opening for the same area as shown in Fig. 11a and b. It can be seen that the crack path clearly follows the regions where mainly NGs are present (indicated by arrows). These volumes have smaller resistance against crack opening due to the weaker particle bonding and the higher porosity caused by the incomplete sintering owing to the large fraction of NiO on the interfaces of NGs. The behavior of these small

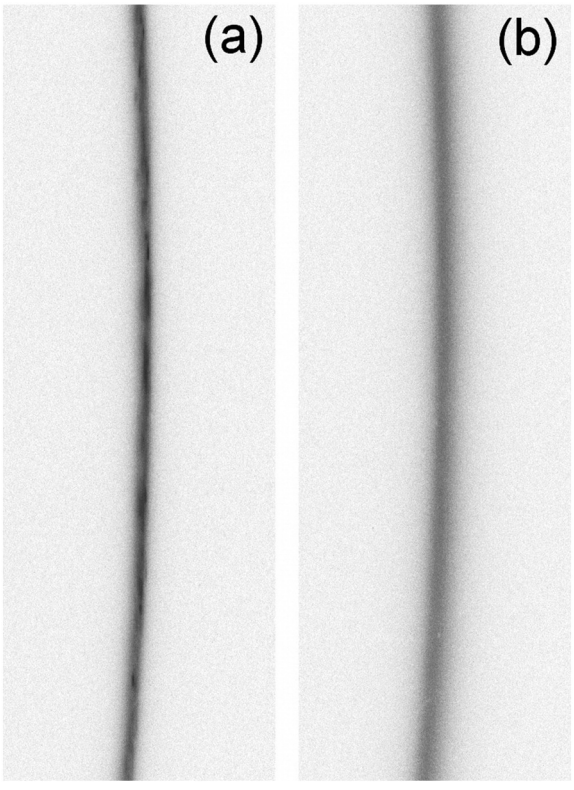

Fig. 9. Debye–Scherrer diffraction rings for reflection 200 in the case of the initial state (a) and after its deformation up to the strain of ~32% (b) at a strain rate of 2×10^{-4} s^{-1}.

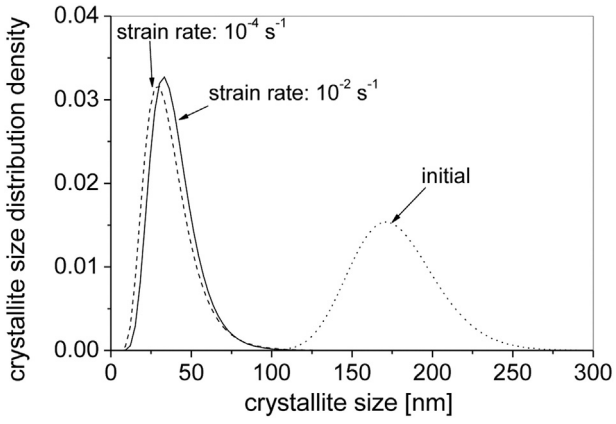

Fig. 10. The crystallite size distributions for the initial sample as well as after compression at the two different strain rates.

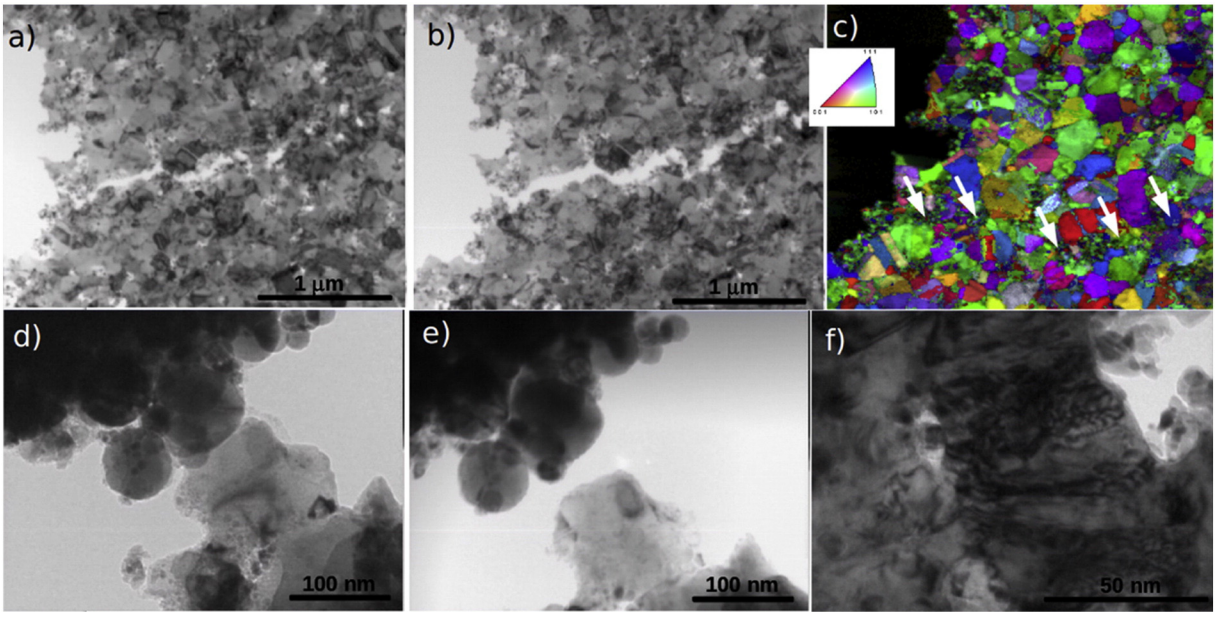

Fig. 11. In-situ TEM experiments showing: evidence of crack propagation by void nucleation and growth in NG area (highlighted by arrows in the orientation map in (c)) (a–c); crack opening by the simple glide of NGs without deformation (d, e); a high dislocation storage in UFG grains in the crack path (f).

grains during crack opening has been monitored, as shown in Fig. 11d and e. These two snapshots taken during straining show that NGs simply glide on each other, confirming the interpretations of the relatively high strain rate sensitivity and the spherical shape of NGs after deformation (see Section 3.2 and Fig. 8).

In addition, a crack may encounter larger UFG grains in its path which may retard the crack growth [3]. This behavior can be noticed in Fig. 11f where there is a UFG grain in a crack path which deforms by multiplication of dislocations. This observation is in agreement with XLPA results which indicated the increase of the average dislocation density during compression. Kumar et al. [38,39] discussed the mechanisms of crack-growth and propagation in NC metals and alloys. In particular, for electrodeposited NC Ni, it was reported that voids at GBs and triple junctions ahead of the main crack grew with progressive loading, thereby producing intergranular fracture. In the present material such mechanisms are facilitated by the pre-existing porosity due to incomplete particle bonding. Finally, it should be noted that our observations are also in line with molecular statics study of the crack propagation in the model material of NC Ni with a mean grain size of 10 nm [40]. It has been shown that the crack propagates inter-

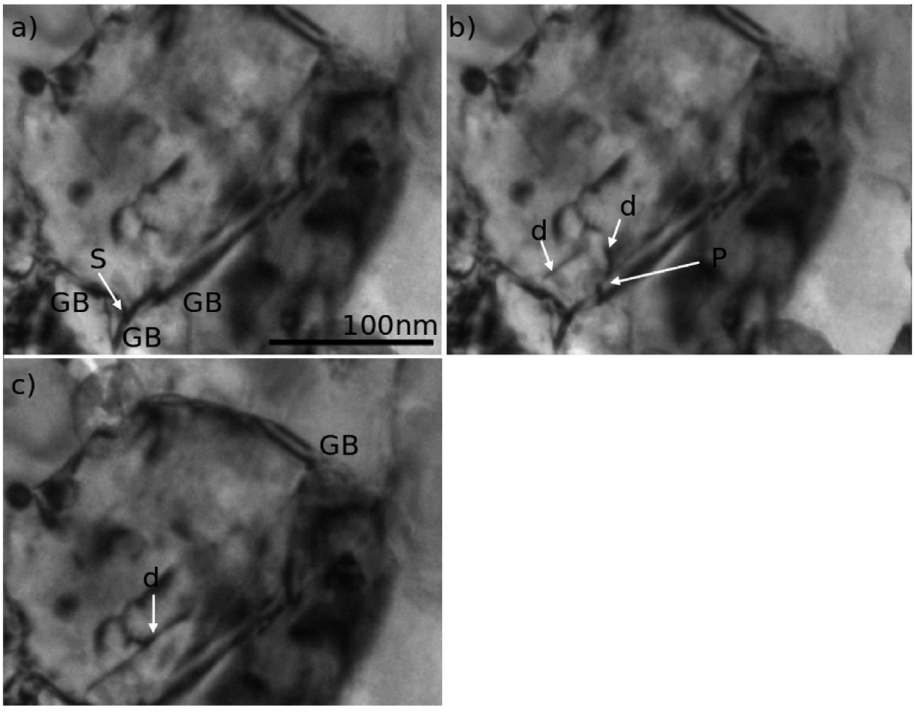

Fig. 12. An inter-granular source (S) operation from a triple junction during an in-situ TEM test close to crack tip (a); a dislocation d is emitted from S and is temporary pinned at a GB (b), before being released and eventually trapped in the opposite GB (c).

granularly, creating nano-voids ahead of the crack which coalesce gradually.

3.4.2. Dislocation emission, pile-up and annihilation

Fig. 12 proves the occurrence of dislocation-based mechanisms of plasticity in a UFG region with negligible porosity. Dislocation emission from both GBs (see Fig. 12, and Supplementary video 1) and intra-granular sources (see Fig. 13 and Supplementary video 2) was detected. These dislocations form pileups inside the grains (see Fig. 13).

Fig. 12a shows a UFG grain with the size of about 200 nm near a crack tip where a high concentration of stresses arises. In the bottom part of the image a dislocation source (denoted by S) can be identified at a triple junction. Upon straining, a dislocation denoted by d is emitted from S and eventually stops at the pinning point P located in a GB. This observation is in agreement with former atomistic simulations, which showed that in NGs the nucleation and the pinning of dislocations occurred at GBs [41]. The operation of dislocation sources at GBs has also been observed in UFG Al thin films [42]. During further straining the curved part of the dislocation is released and glides rapidly toward the opposite GB where it disappears (see Fig. 12c).

An intra-granular source has also been observed during its operation in a grain with the size of about 200 nm (see Fig. 13). This source is a typical single arm source [43] composed of a fixed pining point (PP) and a moving arm (MA) as shown in Fig. 13a. Upon straining, the moving arm expands around the fixed point and a dislocation (denoted by d4 in Fig. 13b) is generated. This dislocation further glides toward a GB. From the previously generated dislocations (denoted by d1, d2 and d3) a pile-up formed in front of the GB. It seems that the stress field of dislocation d4 resulted in a decrease of the spacing between dislocations d1–d3 and the GB. This source has been observed to operate several times before stopping. However, after a few tens of seconds the dislocation in front of the pile-up was gradually absorbed by the GB as a consequence of stress delocalization in the GB [44,45]. Previous in-situ work on NC Ni [38] revealed copious dislocation emission triggered at crack tips, and this process extended over several grains ahead of the tip. In addition, the authors showed that these dislocations generated at GBs and were absorbed at the opposite or adjacent boundary. Even if the considered grain size regime was narrow (30–40 nm), these observations are in line with the findings of the present work. Due to the dislocation absorption in GBs, the back stress exerted by the GBs on the pile-up and the source, which is proportional to the number of dislocations, decreases and the emission process can continue. The absorption of dislocations at GBs is thermally activated and thus may contribute to the observed strain rate sensitivity [46]. At low strain rates, the thermally activated annihilation of dislocations can compensate the dislocation emission from the sources, resulting in a moderate hardening. However, with increasing strain rates the annihilated dislocation density per unit strain decreased which yielded higher dislocation density, leading to a larger strain hardening [45].

3.4.3. Twinning and partial dislocation activity

On the one hand, EBSD and TEM investigations showed the presence of grown-in twins in the as-consolidated Ni microstructures. On the other hand, in normal conditions, deformation twinning is not a preferential deformation mode in Ni because of its quite high stacking fault energy (SFE). However, at high stress levels the required local stress for twinning can be achieved. This situation can be easily fulfilled at crack tip where copious fine twins can be observed, as shown in Fig. 14 (note that the grain labeled as A has already been shown in Figs. 12 and 13 with operating dislocation sources). Molecular statics predicted such events [40] and recently Kumar et al. [38] also reported the formation of twins during deformation of electrodeposited NC Ni in a TEM. But as discussed in Ref. [39], care must be exercised to differentiate between deformation and growth twins. This is also the case in the present study, as growth twins already exist within the as-consolidated microstructure. Indeed, as discussed above, EBSD investigations showed that in the course of deformation the amount of TBs decreased (actually all CSL-type Σ3 boundaries, including TBs). In addition, XLPA showed that the TB probability decreased from about 0.5 to 0.1–0.2% (see Table 1) which suggests an un-twinning process in the course of straining. Additionally, our in-situ TEM experiments revealed the motion of partial dislocations inside the nano-twins as illustrated in Fig. 14b–c as well as in Supplementary video 3. Indeed, Fig. 14b and c shows two snapshots taken during straining in a grain located between two pores (visible on the left and right sides of the images) along the crack path. A subgrain boundary (SGB) connected to a twin (T) is also visible. A partial dislocation (denoted by d) presumably emitted from the SGB can be clearly identified in the twin, as it induces a typical shift in the twin fringes apart from the dislocation (see how the black and white fringes are not in correspondence across the dislocation in the inset of Fig. 14b). Upon straining, the partial dislocation moves rapidly along the twin extending the fault from left to right (Fig. 14c). Note that in the inset of Fig. 14c the fault fringes become continuous in contrast to Fig. 14b. It is emphasized that the extension of the twinned volume by partial dislocation glide does not increase the twin boundary probability. The overall decrease of the twin boundary probability observed by EBSD and XLPA (i.e. the detwinning) might be related to the large increase of dislocation density during deformation that can copiously interact with growth twins, leading to a TB disruption and coherency loss as reported in Refs. [32,39,47].

4. Conclusions

- A bulk polycrystalline nickel sample was processed by SPS from a heterogeneous powder consisting of a mixture of nano- and micrometer-sized particles. The consolidated sample has a bimodal grain structure comprising ~55 vol.% CG and ~45 vol.% UFG components. The CG volumes can be subdivided into two fractions: isolated micrometer-sized grains with an average grain size of ~2 μm and larger spherical multi-

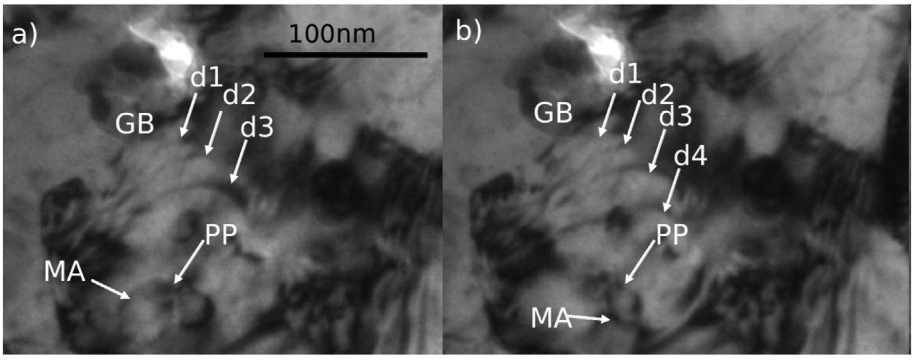

Fig. 13. Operation of an intra-granular single arm source in a UFG grain followed during an in-situ TEM tensile test. The source is composed of a pinning point (PP) around which a mobile arm (MA) expands and produces dislocations d1–d4 piling against a GB (a, b).

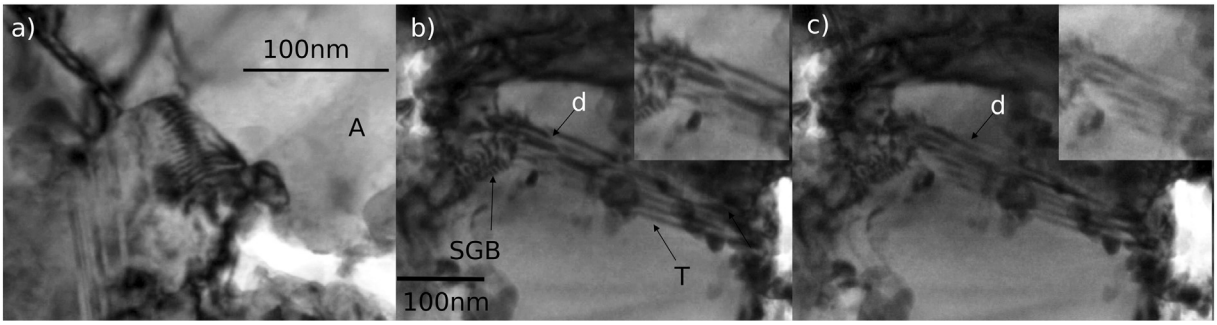

Fig. 14. Nanotwins observed at the crack tip near grain A where intense dislocation activity has been noticed (a); a partial dislocation (denoted by d) motion in a twin (denoted by T) along the crack path (b, c). The inset in (c) shows the change in the fringe contrast of the twin before and after the dislocation motion.

crystalline clusters with the size of ~30 μm, which occupy 51 and 4 vol.% of the whole microstructure, respectively.

- During compression the crystallite size decreased, the dislocation density and the LAGB fraction increased while the twin boundary frequency decreased, which indicate that dislocations have significant contribution to plastic deformation in this consolidated bimodal microstructure. In-situ TEM observations during tensile test also showed the operation of dislocation sources in the interior and in the boundaries of UFG grains.
- Besides dislocation activity, gliding and rolling of NGs were also observed during deformation. The dislocation activity in CG volumes of the consolidated bimodal microstructure might yield an increase of strain hardening capability, contributing also to the observed high strain rate sensitivity.
- It seems that the native NiO phase on the surface of nanoparticles hindered the consolidation in the regions consisting of NGs. Therefore, the cracks formed during deformation usually propagated in these regions which have smaller resistance against crack opening due to the weaker particle bonding and porosity. In nanograin clusters in-situ TEM revealed the occurrence of twinning, partial dislocation activity and rolling of NGs at crack tips.

Supplementary data to this article can be found online at http://dx.doi.org/10.1016/j.matchar.2014.11.025.

Acknowledgments

This work was carried out in the framework of the “MIMIC” project funded by the French National Research Agency, ANR-09-BLAN-0010 and “Investissement d'Avenir” program reference ANR-10-EQPX-38-01. This work was supported in part by the Hungarian Scientific Research Fund, OTKA, Grant No. K-109021. This work has been supported by the French National Research Agency under the “Investissement d'Avenir” program reference No. ANR-10-EQPX-38-01.

References

[1] H. Gleiter, Nanocrystalline materials, Prog. Mater. Sci. 33 (1989) 223–315, http://dx.doi.org/10.1016/0079-6425(89)90001-7.
[2] R.Z. Valiev, R.K. Islamgaliev, I.V. Alexandrov, Bulk nanostructured materials from severe plastic deformation, Prog. Mater. Sci. 45 (2000) 103–189, http://dx.doi.org/10.1016/S0079-6425(99)00007-9.
[3] S. Billard, J. Fondere, B. Bacroix, G. Dirras, Macroscopic and microscopic aspects of the deformation and fracture mechanisms of ultrafine-grained aluminum processed by hot isostatic pressing, Acta Mater. 54 (2006) 411–421, http://dx.doi.org/10.1016/j.actamat.2005.09.012.
[4] W. Cao, G. Dirras, M. Benyoucef, B. Bacroix, Room temperature deformation mechanisms in ultrafine-grained materials processed by hot isostatic pressing, Mater. Sci. Eng. A 462 (2007) 100–105, http://dx.doi.org/10.1016/j.msea.2006.04.155.
[5] V. Haas, H. Gleiter, R. Birringer, Synthesis of nanostructured materials by the use of a thermophoretic forced flux system, Scr. Metall. Mater. 28 (1993) 721–724, http://dx.doi.org/10.1016/0956-716X(93)90041-P.
[6] G. Dirras, S. Bouvier, J. Gubicza, B. Hasni, T. Szilagyi, Mechanical characteristics under monotonic and cyclic simple shear of spark plasma sintered ultrafine-grained nickel, Mater. Sci. Eng. A 526 (2009) 201–210, http://dx.doi.org/10.1016/j.msea.2009.07.034.
[7] B. Srinivasarao, K. Oh-ishi, T. Ohkubo, K. Hono, Bimodally grained high-strength Fe fabricated by mechanical alloying and spark plasma sintering, Acta Mater. 57 (2009) 3277–3286, http://dx.doi.org/10.1016/j.actamat.2009.03.034.
[8] S. Paris, E. Gaffet, F. Bernard, Z.A. Munir, Spark plasma synthesis from mechanically activated powders: a versatile route for producing dense nanostructured iron aluminides, Scr. Mater. 50 (2004) 691–696, http://dx.doi.org/10.1016/j.scriptamat.2003.11.019.
[9] Y.M. Wang, E. Ma, Three strategies to achieve uniform tensile deformation in a nanostructured metal, Acta Mater. 52 (2004) 1699–1709, http://dx.doi.org/10.1016/j.actamat.2003.12.022.
[10] A.A. Fedorov, M.Y. Gutkin, I.A. Ovid'ko, Triple junction diffusion and plastic flow in fine-grained materials, Scr. Mater. 47 (2002) 51–55, http://dx.doi.org/10.1016/S1359-6462(02)00096-9.
[11] M. Dao, L. Lu, R.J. Asaro, J.T.M. De Hosson, E.J. Ma, Toward a quantitative understanding of mechanical behavior of nanocrystalline metals, Acta Mater. 55 (2007) 4041–4065, http://dx.doi.org/10.1016/j.actamat.2007.01.038.
[12] M. Dao, L. Lu, Y.F. Shen, S. Suresh, Strength, strain-rate sensitivity and ductility of copper with nanoscale twins, Acta Mater. 54 (2006) 5421–5432, http://dx.doi.org/10.1016/j.actamat.2006.06.062.
[13] L. Lu, R. Schwaiger, Z. Shan, M. Dao, K. Lu, S. Suresh, Nano-sized twins induce high rate sensitivity of flow stress in pure copper, Acta Mater. 53 (2005) 2169–2179, http://dx.doi.org/10.1016/j.actamat.2005.01.031.
[14] R. Schwaiger, B. Moser, M. Dao, N. Chollacoop, S. Suresh, Some critical experiments on the strain-rate sensitivity of nanocrystalline nickel, Acta Mater. 51 (2003) 5159–5172, http://dx.doi.org/10.1016/S1359-6454(03)00365-3.
[15] B. Ahn, E.J. Lavernia, S.R. Nutt, Dynamic observations of deformation in an ultrafine-grained Al–Mg alloy with bimodal grain structure, J. Mater. Sci. 43 (2008) 7403–7408, http://dx.doi.org/10.1007/s10853-008-2950-1.
[16] A.P. Newbery, B. Ahn, P. Pao, S.R. Nutt, E.J. Lavernia, A ductile UFG Al alloy via cryomilling and quasi-isostatic forging, Adv. Mater. Res. 29–30 (2007) 21–29, http://dx.doi.org/10.4028/www.scientific.net/AMR.29-30.21.
[17] L. Farbaniec, G. Dirras, A. Krawczynska, F. Mompiou, H. Couque, F. Naimi, F. Bernard, D. Tingaud, Powder metallurgy processing and deformation characteristics of bulk multimodal nickel, Mater. Charact. 94 (2014) 26–137, http://dx.doi.org/10.1016/j.matchar.2014.05.008.
[18] K. Sitarama Raju, V. Subramanya Sarma, A. Kauffmann, Z. Hegedűs, J. Gubicza, M. Peterlechner, J. Freudenberger, G. Wilde, High strength and ductile ultrafine-grained Cu–Ag alloy through bimodal grain size, dislocation density and solute distribution, Acta Mater. 61 (2013) 228–238, http://dx.doi.org/10.1016/j.actamat.2012.09.053.
[19] C. Lu, Y.W. Mai, Y.G. Shen, Recent advances on understanding the origin of superhardness in nanocomposite coatings: a critical review, J. Mater. Sci. 41 (2006) 937–950, http://dx.doi.org/10.1007/s10853-006-6577-9.
[20] V.L. Tellkamp, E.J.J. Lavernia, Processing and mechanical properties of nanocrystalline 5083 Al alloy, Nanostruct. Mater. 12 (1999) 249–252, http://dx.doi.org/10.1016/S0965-9773(99)00110-5.
[21] Y.H. Zhao, T. Topping, J.F. Bingert, J.J. Thornton, A.M. Dangelewicz, Y. Li, W. Liu, Y.T. Zhu, Y.Z. Zhou, E.L. Lavernia, High tensile ductility and strength in bulk nanostructured nickel, Adv. Mater. 20 (2008) 3028–3033, http://dx.doi.org/10.1002/adma.200800214.
[22] V.Y. Gertsman, R. Birringer, On the room-temperature grain growth in nanocrystalline copper, Scr. Metall. Mater. 30 (1994) 577–581, http://dx.doi.org/10.1016/0956-716X(94)90432-4.
[23] Y. Estrin, A. Vinogradov, Extreme grain refinement by severe plastic deformation: a wealth of challenging science, Acta Mater. 61 (2013) 782–817, http://dx.doi.org/10.1016/j.actamat.2012.10.038.
[24] Y. Wang, M. Chen, F. Zhou, E. Ma, High tensile ductility in a nanostructured metal, Nature (2002) 419–912, http://dx.doi.org/10.1038/nature01133.
[25] G. Dirras, D. Tingaud, G. Csiszár, J. Gubicza, H. Couque, F. Mompiou, Characterization of bulk bimodal polycrystalline nickel deformed by direct impact loadings, Mater. Sci. Eng. A 601 (2014) 48–57, http://dx.doi.org/10.1016/j.msea.2014.02.043.
[26] F. Tepper, Electro-explosion of wire produces nanosize metals, Met. Powder Rep. 53 (6) (1998) 31–33, http://dx.doi.org/10.1016/S0026-0657(98)80193-8.

[27] R. Orrù, R. Licheri, A.M. Locci, A. Cincotti, G. Cao, Consolidation/synthesis of materials by electric current activated/assisted sintering, Mater. Sci. Eng. R. Rep. 63 (2009) 127–287, http://dx.doi.org/10.1016/j.mser.2008.09.003.
[28] G.D. Dutel, D. Tingaud, P. Langlois, G. Dirras, Room-temperature deformation micromechanisms of polycrystalline nickel processed by spark plasma sintering, Mater. Charact. 79 (2013) 76–83, http://dx.doi.org/10.1016/j.matchar.2013.02.013.
[29] G. Ribárik, J. Gubicza, T. Ungár, Correlation between strength and microstructure of ball-milled Al–Mg alloys determined by X-ray diffraction, Mater. Sci. Eng. A 387–389 (2004) 343–347, http://dx.doi.org/10.1016/j.msea.2004.01.089.
[30] L. Balogh, G. Tichy, T. Ungár, Twinning on pyramidal planes in hexagonal close packed crystals determined along with other defects by X-ray line profile analysis, J. Appl. Crystallogr. 42 (2009) 580–591, http://dx.doi.org/10.1107/S0021889809022936.
[31] L. Veleva, R. Schäublin, A. Ramar, Z. Oksiuta, N. Baluc, in: S. Richter, A. Schwedt (Eds.), Focused Ion Beam Application on the Investigation of Tungsten-Based Materials for Fusion Application, Springer-Verlag Publication, Berlin Heidelberg, 2008, pp. 503–504, http://dx.doi.org/10.1007/978-3-540-85226-1_252.
[32] A. Coujou, P. Lours, N.A. Roy, D. Caillard, N. Clément, Determination of the local tensile axis direction in a TEM in situ strained γ′ single crystal—a finite element approach, Acta Mater. 38 (1990) 825–837, http://dx.doi.org/10.1016/0956-7151(90)90036-G.
[33] E.F. Rauch, M. Véron, J. Portillo, D. Bultreys, Y. Maniette, S. Nicolopoulos, Automatic crystal orientation and phase mapping in TEM by precession diffraction, Microsc. Anal. 22 (2008) S5–S8.
[34] J. Gubicza, X-ray Line Profile Analysis in Materials Science, IGI-Global, Hershey, PA, USA, 2014., http://dx.doi.org/10.4018/978-1-4666-5852-3.
[35] J. Gubicza, H.-Q. Bui, F. Fellah, G. Dirras, Microstructure and mechanical behavior of ultrafine-grained Ni processed by different powder metallurgy methods, J. Mater. Res. 24 (2009) 217–226, http://dx.doi.org/10.1557/JMR.2009.0010.
[36] R.J. Asaro, S. Suresh, Mechanistic models for the activation volume and rate sensitivity in metals with nanocrystalline grains and nano-scale twins, Acta Mater. 53 (2005) 3369–3382, http://dx.doi.org/10.1016/j.actamat.2005.03.047.
[37] H. Conrad, Grain-size dependence of the flow stress of Cu from millimeters to nanometers, Metall. Mater. Trans. A 35A (2004) 2681–2695, http://dx.doi.org/10.1007/s11661-004-0214-5.
[38] K.S. Kumar, S. Suresh, M.F. Chisholm, J.A. Horton, P. Wang, Deformation of electrodeposited nanocrystalline nickel, Acta Mater. 51 (2003) 387–405, http://dx.doi.org/10.1016/S1359-6454(02)00421-4.
[39] K.S. Kumar, H. Van Swygenhoven, S. Suresh, Mechanical behavior of nanocrystalline metals and alloys, Acta Mater. 51 (2003) 5743–5774, http://dx.doi.org/10.1016/j.actamat.2003.08.032.
[40] D. Farkas, S. Van Petegem, P.M. Derlet, H. Van Swygenhoven, Dislocation activity and nano-void formation near crack tips in nanocrystalline Ni, Acta Mater. 53 (2005) 3115–3123, http://dx.doi.org/10.1016/j.actamat.2005.02.012.
[41] H. Van Swygenhoven, Footprints of plastic deformation in nanocrystalline metals, Mater. Sci. Eng. A 483–484 (2008) 33–39, http://dx.doi.org/10.1016/j.msea.2006.10.204.
[42] F. Mompiou, M. Legros, A. Boé, M. Coulombier, J.-P. Raskin, T. Pardoen, Inter- and intragranular plasticity mechanisms in ultrafine-grained Al thin films: an in situ TEM study, Acta Mater. 61 (2013) 205–216, http://dx.doi.org/10.1016/j.actamat.2012.09.051.
[43] F. Mompiou, M. Legros, A. Sedlmayr, D.S. Gianola, D. Caillard, O. Kraft, Source-based strengthening of sub-micrometer Al fibers, Acta Mater. 60 (2012) 977–983, http://dx.doi.org/10.1016/j.actamat.2011.11.005.
[44] P.H. Humphreys, H. Gleiter, The annealing of dislocations in high-angle grain boundaries, Philos. Mag. 30 (1974) 593–602, http://dx.doi.org/10.1080/14786439808206584.
[45] F. Mompiou, D. Caillard, M. Legros, H. Mughrabi, In situ TEM observations of reverse dislocation motion upon unloading in tensile-deformed UFG aluminium, Acta Mater. 60 (2012) 3402–3414, http://dx.doi.org/10.1016/j.actamat.2012.02.049.
[46] J. Kwiecinski, J.W. Wyrzykowski, Kinetics of recovery on grain boundaries in polycrystalline aluminium, Acta Metall. 37 (1989) 1503–1507, http://dx.doi.org/10.1016/0001-6160(89)90182-X.
[47] Y.T. Zhu, X.Z. Liao, X.L. Wu, J. Narayan, Grain size effect on deformation twinning and detwinning, J. Mater. Sci. 48 (2013) 4467–4475, http://dx.doi.org/10.1007/s10853-013-7140-0.